ADVANCED ENERGY MATERIALS
www.advenergymat.de

FeS_2 Nanoparticles Embedded in Reduced Graphene Oxide toward Robust, High-Performance Electrocatalysts

*Yanan Chen, Shaomao Xu, Yuanchang Li, Rohit Jiji Jacob, Yudi Kuang, Boyang Liu, Yilin Wang, Glenn Pastel, Lourdes G. Salamanca-Riba, Michael R. Zachariah, and Liangbing Hu**

Developing low-cost, highly efficient, and robust earth-abundant electrocatalysts for hydrogen evolution reaction (HER) is critical for the scalable production of clean and sustainable hydrogen fuel through electrochemical water splitting. This study presents a facile approach for the synthesis of nanostructured pyrite-phase transition metal dichalcogenides as highly active, earth-abundant catalysts in electrochemical hydrogen production. Iron disulfide (FeS_2) nanoparticles are in situ loaded and stabilized on reduced graphene oxide (RGO) through a current-induced high-temperature rapid thermal shock (≈12 ms) of crushed iron pyrite powder. FeS_2 nanoparticles embedded in between RGO exhibit remarkably improved electrocatalytic performance for HER, achieving 10 mA cm^{-2} current at an overpotential as low as 139 mV versus a reversible hydrogen electrode with outstanding long-term stability under acidic conditions. The presented strategy for the design and synthesis of highly active earth-abundant nanomaterial catalysts paves the way for low-cost and large-scale electrochemical energy applications.

1. Introduction

With the ever-rising global demand for energy and growth of serious environmental issues associated with energy consumption, the production and exploration of clean and sustainable energy are imminent. Hydrogen is a promising alternative energy due to its highest energy density among all fuels and completely clean combustion process in which only water and energy are produced without any by-products. Electrochemical/photoelectrochemical water splitting is one of the most attractive strategies to produce hydrogen among the existing methods for hydrogen fuel production.[1–6] Currently, the state-of-the-art catalyst for hydrogen evolution reaction (HER) is platinum (Pt), a noble metal, which can reach a current density of 100 mA cm^{-2} with a small overpotential of ≈50 mV.[7,8] However, the high cost and low elemental abundance of this noble metal inhibit large-scale hydrogen production and application. Therefore, numerous research efforts have been devoted to developing cost-effective, earth-abundant electrocatalysts with high HER activity.[9–18] Various materials based on earth-abundant elements, such as MoS_2,[19–23] amorphous MoS_x,[24,25] MoC_2,[11,15] MoC_x,[8] $MoSe_2$,[26] WS_2,[27,28] WC,[29] WSe_2,[30] CoPS,[31,32] $NiFeO_x$,[33] Ni_3S_2,[34] Ni_2P,[35] $NiMoN_x$,[36] and Ni-Mo alloy,[37] are promising HER catalysts. For example, Cui and co-workers demonstrated that electrochemically tuned MoS_2 nanoparticles achieved 200 mA cm^{-2} cathodic current at only 200 mV overpotential.[38]

Among these various earth-abundant electrocatalysts for HER, the cubic pyrite-phase transition metal dichalcogenides, such as iron disulfide (iron pyrite, FeS_2), are emerging as a new generation of low-cost, highly active alternatives. FeS_2 has been widely investigated as catalysts for energy storage and conversion applications due to the great abundance of iron pyrite minerals.[39,40] Specifically, nanostructured FeS_2 is presently under extensive investigation as low-cost solar absorbers,[41] catalysts for oxygen reduction reaction[42] and electrode materials in batteries.[43] In addition, nanostructured FeS_2 has been studied as a highly active electrocatalyst for HER.[40,44] A recent work demonstrated that 10 mA cm^{-2} current was achieved at ≈260 mV overpotential using FeS_2 thin film as a catalyst in 0.5 M H_2SO_4 solution.[44] The FeS_2 thin film was synthesized by treating e-beam evaporated Fe thin films through a sulfurization reaction. Although progress has been made on investigating and designing efficient and cost-effective catalyst for HER, the synthesis methods for nanostructured catalysts still need to be improved greatly in order to realize fast, low-cost, and scalable nanomanufacturing for catalysts.

In this work, we present a facile strategy to synthesize FeS_2 nanoparticles derived from iron pyrite as highly efficient and stable electrocatalysts for water splitting. We use FeS_2 powders derived from iron pyrite and graphene oxide flakes exfoliated

Dr. Y. Chen, Dr. S. Xu, Y. Kuang, B. Liu, Dr. Y. Wang, G. Pastel, Prof. L. G. Salamanca-Riba, Prof. L. Hu
Department of Materials Science and Engineering
University of Maryland College Park
College Park, MD 20742, USA
E-mail: binghu@umd.edu
Prof. Y. Li
National Center for Nanoscience and Technology
Beijing 100190, China
R. J. Jacob, Prof. M. R. Zachariah
Department of Chemical and Biomolecular Engineering and Chemistry and Biochemistry
University of Maryland College Park
College Park, MD 20742, USA

DOI: 10.1002/aenm.201700482

 © 2017 WILEY-VCH Verlag GmbH & Co. KGaA, Weinheim

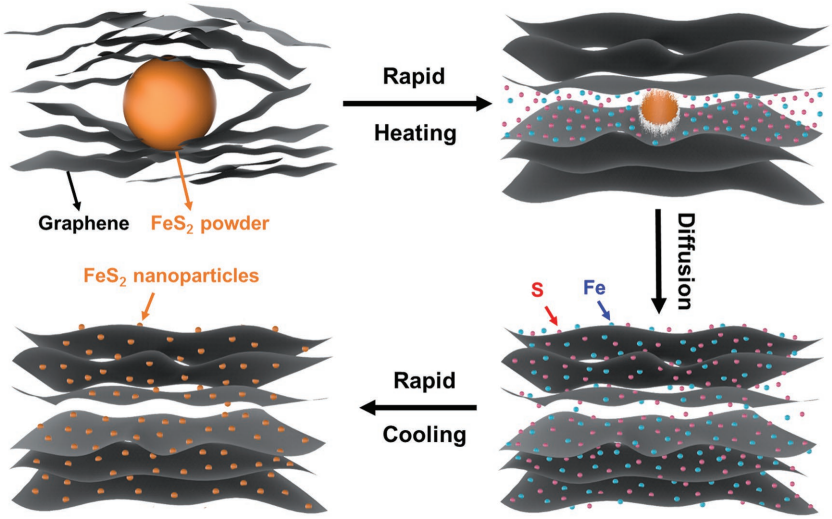

Figure 1. Schematic illustration of the ultrafast, in situ transformation of minerals to catalyst nanoparticles. FeS_2 powders and reduced graphene oxide (RGO) flakes derived from iron pyrite and graphite as raw materials can be transformed into ultrafine FeS_2 nanoparticles (10–20 nm). The ultrafine FeS_2 nanoparticles are uniformly distributed on the RGO nanosheets and the transformation process is completed in an ultrashort time (≈12 ms) through direct high-temperature treatment (≈2470 K). The proposed mechanism for nanoparticle formation entails FeS_2 powder decomposition into Fe and S atoms upon rapid heating and recrystallization upon rapid cooling.

from graphite through an improved Hummers' method[45,46] as raw materials to fabricate micro-FeS_2-RGO films. The nano-FeS_2-RGO is then in situ synthesized by directly joule heating the as-prepared micro-FeS_2-RGO film to a high temperature (≈2470 K) in a short time (≈12 ms). The process is defined as a thermal shock in this study. After thermal shock treatment, FeS_2 nanoparticles (10–20 nm) are uniformly distributed on RGO nanosheets, as illustrated schematically in **Figure 1**. The following mechanism is proposed for ultrafast, in situ FeS_2 nanoparticle formation on RGO at high temperatures. FeS_2 powders decompose into Fe and S atoms in the rapid heating process up to 2470 K.[47] The Fe and S atoms then diffuse within the RGO matrix but remain in between the RGO layers under high temperature thereby benefiting from the impermeability of RGO[48] and the encapsulation effect of the RGO film. As rapid cooling takes place, the Fe and S atoms renucleate around the defects on the basal plane of the RGO nanosheets and crystallize into ultrafine FeS_2 nanoparticles (Figure 1). The FeS_2-RGO 3D nanostructure we designed helps to maintain good mechanical integration and rapid electron transport of FeS_2 nanoparticles embedded in the RGO nanosheets. This unique method enables in situ synthesis of FeS_2 nanoparticles in an ultrafast, cost-effective, and scalable approach. As a proof of concept, we demonstrated that FeS_2 nanoparticles transformed from iron pyrite through ultrafast thermal shock can be used as catalysts to split water. Benefiting from the ultrafine FeS_2 nanoparticles and the robust FeS_2-RGO 3D structure, the as-synthesized nano-FeS_2-RGO exhibits remarkable electrocatalytic performance for HER with only 139 mV overpotential to achieve 10 mA cm^{-2} current in 0.5 M H_2SO_4 solution for long-term operation. The present strategy is also applicable to synthesize other transition metal dichalcogenides and can even be extended to ternary or multicomponent compounds.

The pristine pyrite mineral is displayed as the inset image in **Figure 2**a, which shows a specimen several centimeters long. After breaking the mineral with a hammer, ≈50 µm FeS_2 particles can be obtained (Figure 2a). To have better control of the particle size in the experiments, commercial micro-sized FeS_2 powder (≈44 µm) and graphene oxide were chosen as raw materials to fabricate the micro-FeS_2-RGO film (Figure 2b) by vacuum filtration followed by thermal annealing at 573 K for 1 h in argon. The obtained freestanding micro-FeS_2-RGO film was then used to synthesize FeS_2 nanoparticles embedded within the RGO film through current-induced thermal shock. The current triggered thermal shock treatment was conducted at a high temperature of 2470 K and the whole process was finished within around 12 ms as shown in the temperature profiles (Figure 2c). The temperature profiles were extracted by fitting the emission spectrum (in the wavelength range of 505–811 nm) from heating the nano-FeS_2-RGO film to Planck's law for blackbody radiation (Figure 2d). The film did not show any obvious change after thermal shock from the appearance point of view (Figure S1, Supporting Information). The morphology of the as-synthesized FeS_2 nanoparticles after thermal shock treatment is shown in Figure 2e where the FeS_2 nanoparticles are 10–20 nm in diameter (Figure S2, Supporting Information) and evenly distributed on the RGO nanosheets. A close view image in the inset of Figure 2e shows that most of the nanoparticles stabilized on the RGO are spherical or subsphaeroidal in shape (Figure S3, Supporting Information). Energy-dispersive X-ray spectroscopy (EDX) of a single nanoparticle presents the elements C, Fe, and S with an S/Fe atomic ratio of ≈2.0 (Figure 2f), suggesting the iron-sulfide nanoparticle is FeS_2.

Transmission electron microscopy (TEM) further reveals the structure of the as-synthesized FeS_2 and RGO nanocomposite (**Figure 3**). TEM images show the typical spherical morphology of FeS_2 nanoparticles with an average size of 10–20 nm distributed on wrinkled 2D RGO nanosheets (Figure 3a). Figure 3b, the enlarged TEM image, illustrates that FeS_2 nanoparticles were uniformly embedded in the RGO nanosheets. High-resolution TEM shows lattice plane spacing of 0.22 nm (Figure 3c), which corresponds to the (211) crystal planes of the pyrite structure, indicating excellent crystallinity of the as-synthesized FeS_2 nanoparticles. The EDX elemental mapping of as-synthesized FeS_2 nanoparticles reveals the distribution of Fe and S elements over the whole nanoparticle on the RGO nanosheet (Figure 3d–f). The crystallinity of the FeS_2 nanoparticles embedded between RGO sheets is further confirmed by X-ray diffraction (XRD). The XRD spectrum shows a broad RGO peak at ≈26° corresponding to the C (002) plane, and dominant sharp diffraction peaks at ≈33°, 41°, and 59° ascribed to the reflection of (200), (211), and (222) planes of pyrite FeS_2, which is consistent with the TEM results (Figure S4, Supporting Information).

© 2017 WILEY-VCH Verlag GmbH & Co. KGaA, Weinheim

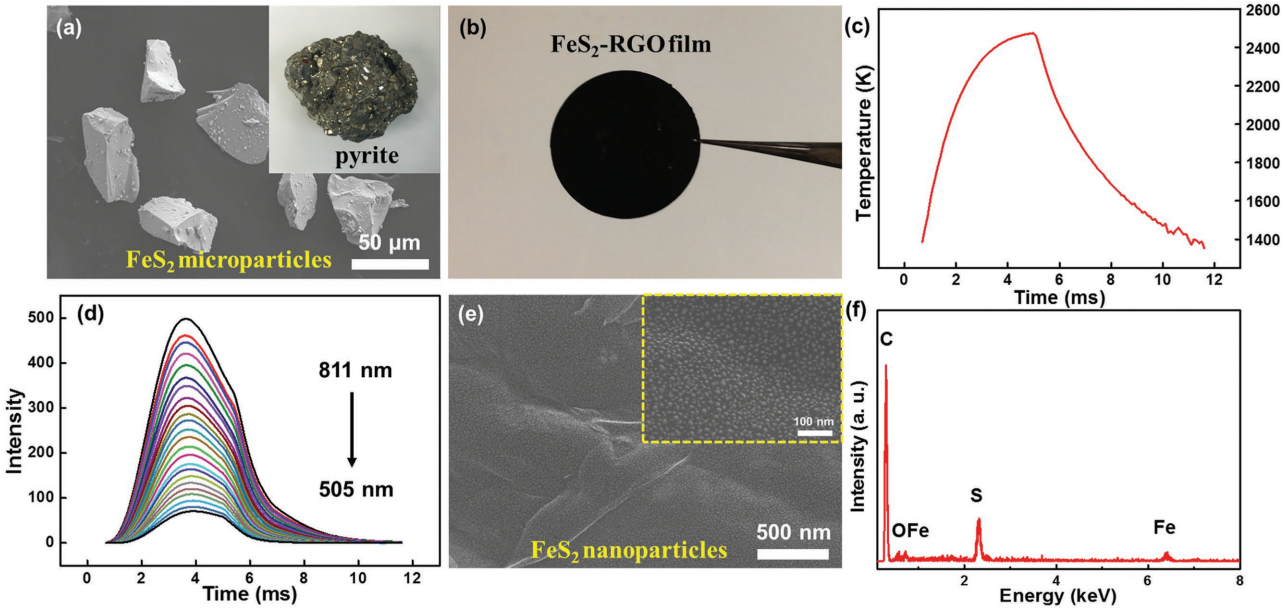

Figure 2. Characterizations of pyrite and FeS_2 nanoparticles. a) FESEM image of FeS_2 powders broken from pyrite. The inset shows the pristine pyrite. b) Digital image of fabricated FeS_2-RGO film. c) Temperature profile during the high-temperature synthesis of nano-FeS_2-RGO. d) Emission spectra of nano-FeS_2-RGO film in the wavelength range of 505–811 nm in the ultrafast synthesis process. e) FESEM image of as-synthesized FeS_2 nanoparticles uniformly distributed on RGO nanosheets. The inset shows details of the surface morphology at higher magnification. f) EDX spectrum of nano-FeS_2-RGO.

The chemical composition and electronic states of as-synthesized FeS_2 nanoparticles on RGO nanosheets are investigated by X-ray photoelectron spectroscopy (XPS; **Figure 4**) where all spectra were calibrated to 284.0 according to sp^2 carbon. The survey scan (Figure 4a) shows that the nano-FeS_2-RGO consists mainly of C, O, Fe, and S, where the signals of C and O originate from the RGO nanosheets. The XPS spectrum presents signals of S 2p and Fe 2p with atomic ratios of 3.56% and 1.78%, respectively. Accordingly, an S/Fe ratio of 2.0 can be derived from the XPS results which is close to the S/Fe ratio measured by EDX (Figure 2f). The high-resolution C 1s spectrum can be decoupled into five bands (Figure 4b), which correspond to C=C (284.0 eV), C—C (284.9 eV), C—O (286.5 eV), C=O (287.6 eV), and O—C=O (289.0 eV).[49,50] The characteristic

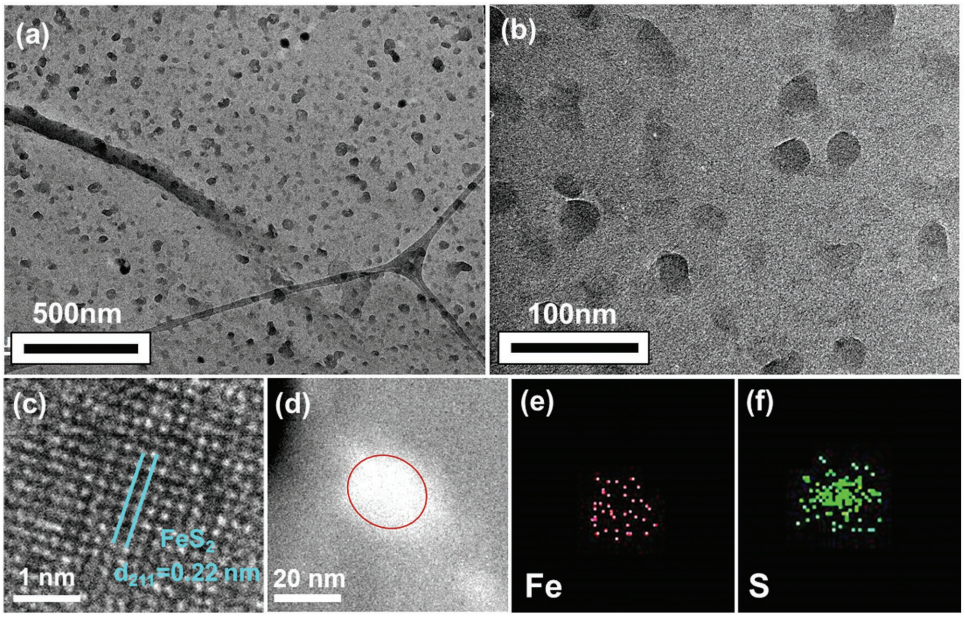

Figure 3. Characterizations of nano-FeS_2-RGO. a) TEM image of FeS_2 nanoparticles on RGO nanosheets. b) Magnified TEM image. c) High-resolution TEM image of a FeS_2 nanoparticle, presenting clear lattice fringes with a lattice plane spacing of 0.22 nm which corresponds to the (211) crystal plane of FeS_2. d–f) High-angle annular dark-field TEM image of an FeS_2 nanoparticle and the corresponding EDX elemental mapping of Fe and S.

 © 2017 WILEY-VCH Verlag GmbH & Co. KGaA, Weinheim

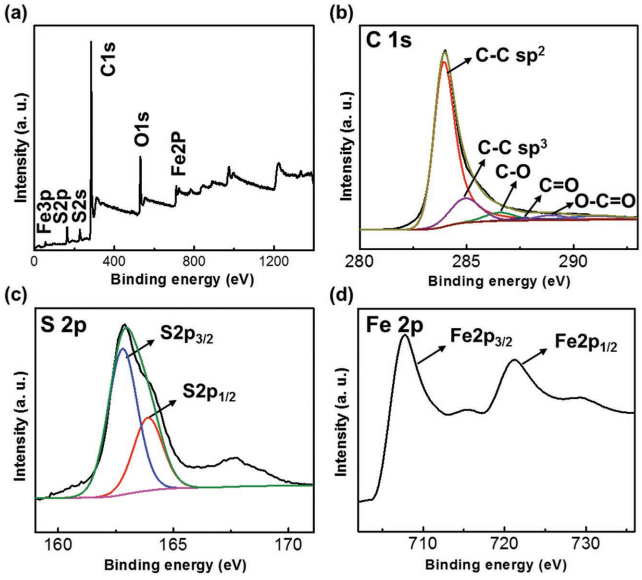

Figure 4. Chemical composition and electronic states characterization of nano-FeS_2-RGO. a) XPS survey spectrum of nano-FeS_2-RGO. b–d) High-resolution XPS spectra of C 1s, S 2p, and Fe 2p for as-synthesized nano-FeS_2-RGO.

peaks of S $2p_{3/2}$ and S $2p_{1/2}$ are observed at binding energies of 162.8 and 163.9 eV (Figure 4c), respectively, which match literature results for FeS_2.[51,52] The high-resolution Fe 2p spectrum reveals two prominent components that can be assigned as Fe $2p_{3/2}$ (707.8 eV) and Fe $2p_{1/2}$ (721.2 eV), which is consistent with the literature values of electron-binding energies of Fe^{2+} cations in FeS_2 (Figure 4d).[51,52] All the aforementioned characterizations confirm the successful synthesis of FeS_2 nanoparticles on RGO nanosheets.

The HER electrocatalytic activity of the synthesized FeS_2 nanoparticles was evaluated in a 0.5 M H_2SO_4 solution employing a typical three-electrode electrochemical system. The direct preparation of FeS_2 nanoparticles grown on RGO nanosheets enables convenient evaluation of its catalytic activity by utilizing the freestanding FeS_2-RGO film as a working electrode. **Figure 5**a shows the cathodic polarization curves of nano-FeS_2-RGO together with micro-FeS_2-RGO as a reference with a mass loading of 1 mg cm^{-2}. The nano-FeS_2-RGO exhibits a much lower onset overpotential of 70 mV versus the reversible hydrogen electrode (RHE) compared with that of micro-FeS_2-RGO (164 mV), which also shows a favorable comparison against other earth-abundant HER electrocatalysts.[53,54] Moreover, the nano-FeS_2-RGO requires a low overpotential of 139 mV versus RHE to achieve significant hydrogen evolution (J = 10 mA cm^{-2}), while micro-FeS_2-RGO requires a high overpotential of 260 mV. The low overpotential of nano-FeS_2-RGO for generating hydrogen from water is among the best reported nonnoble metal electrocatalysts for HER[55,56] (Table S1, Supporting Information). Meanwhile, –100 mA cm^{-2} cathodic current can be observed at a low voltage of –229 mV for nano-FeS_2-RGO, instead of –439 mV for micro-FeS_2-RGO, confirming the greatly improved electrocatalytic activity for nano-FeS_2-RGO. The high HER activity of nano-FeS_2-RGO is further validated by Tafel plots which reflect the current change with increasing potential. The Tafel slope of nano-FeS_2-RGO (66 mV dec^{-1}) is remarkably lower than that of micro-FeS_2-RGO (124 mV dec^{-1}) as depicted in Figure 5b, illustrating the excellent HER catalytic activity of nano-FeS_2-RGO. Although the Tafel slope with a value of 66 mV dec^{-1} is still higher than 30 mV dec^{-1} for Pt-C electrocatalyst, nano-FeS_2-RGO compares favorably to recently reported high-performance earth-abundant HER electrocatalysts.[31,54] In addition, the catalyst exhibits a high turnover frequency of 0.06 s^{-1} per active site at 229 mV overpotential (100 mA cm^{-2}), confirming the excellent intrinsic catalytic activity of nano-FeS_2-RGO (Figure S5, Supporting Information).

Catalytic stability is always a significant criterion for HER catalysts in addition to high electrocatalytic activity. The cycling stability of nano-FeS_2-RGO is investigated by continuous potential sweeping at a scan rate of 50 mV s^{-1} in an acidic electrolyte. The nano-FeS_2-RGO catalyst sustains negligible deterioration of cathodic current after 1000 cycles (Figure 5c), which suggests excellent long-term stability without serious corrosion. Furthermore, the stability of the nano-FeS_2-RGO catalyst is evaluated by catalyzing continuous hydrogen production at a constant overpotential of 170 mV (Figure 5d). The current density of the nano-FeS_2-RGO catalyst remains stable at 24 mA cm^{-2} for more than 10 h in 0.5 M H_2SO_4, confirming the remarkable stability and advantages of FeS_2 nanoparticles embedded in between RGO nanosheets for water splitting. The superior durability of anchored FeS_2 nanoparticles on RGO nanosheets should owe to the strong interaction between FeS_2 catalysts with RGO substrate. RGO film not only acts as a physical support for the catalyst nanoparticles, it also improves the electronic conductivity of the film for efficient water splitting. Moreover, the RGO prevents the loss of nanocatalysts during water splitting.

We also performed first-principles calculations to evaluate the HER activity of FeS_2. In terms of the XRD results, we calculate the Gibbs free energy, ΔG, due to the hydrogen adsorption on the S-terminated (100), (111), and (211) surfaces. Many different S sites are examined and Figure 5e (Figure S6, Supporting Information) plots the results corresponding to the optimal ΔG for the different surfaces which indicates that all three FeS_2 surfaces exhibit catalytic activity (Figures S7–S9, Supporting Information). Nevertheless, the (100) surface deserves particular attention because of its unique geometric configuration and HER process. On the one hand, the S dimerization occurs therein. The absence of dangling bonds implies good structural stability. On the other hand, the free energies are 0.15 and –0.15 eV for the first and second H adsorption, respectively, as illustrated in Figure 5e, which has an overall ΔG of zero resulting in a superior HER activity. Furthermore, the second H prefers the site close to the first one, unambiguously benefitting for their collapse and release. By putting the two together, the FeS_2 (100) surface shows more promising catalytic potential for HER, which provides a theoretical foundation for how the crystal structure of FeS_2 can be optimized for improved catalytic performance.

2. Conclusion

We report a new high-temperature-assisted strategy for synthesizing nanostructured pyrite-phase transition metal

© 2017 WILEY-VCH Verlag GmbH & Co. KGaA, Weinheim

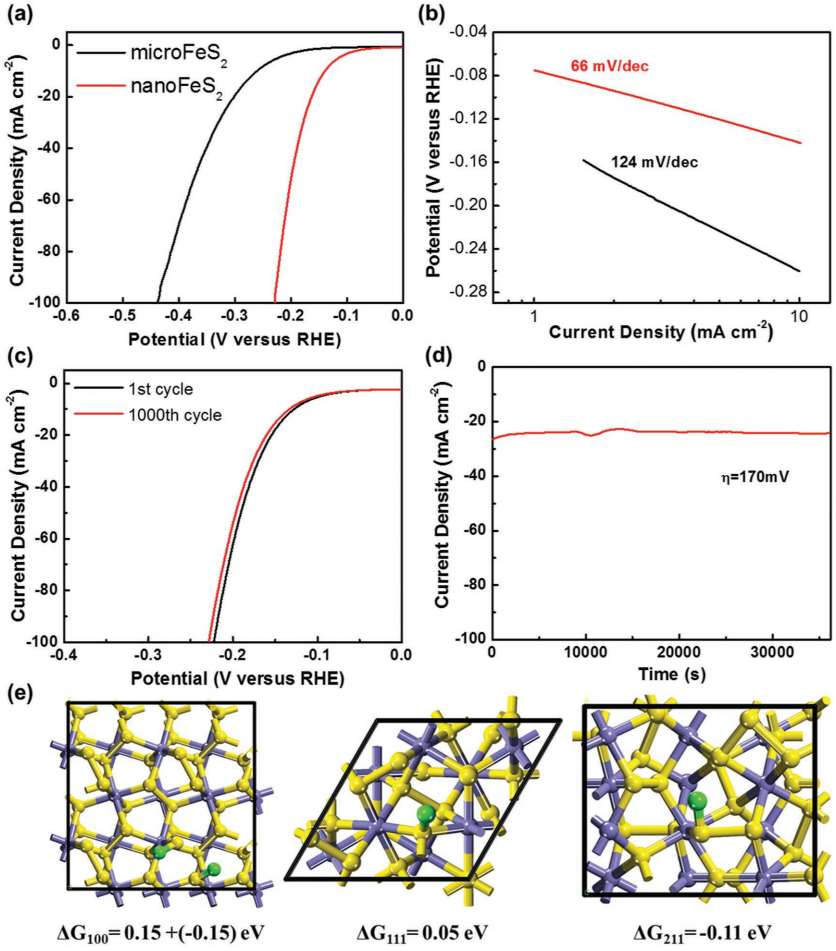

Figure 5. HER electrocatalytic performance of FeS_2 nanoparticles. a) The HER polarization curves of nano-FeS_2-RGO in comparison to micro-FeS_2-RGO at 2 mV s^{-1} in 0.5 M H_2SO_4. b) Corresponding Tafel slopes. c) Cycling stability of nano-FeS_2-RGO after continuous potential sweeps at a scan rate of 50 mV s^{-1} in 0.5 M H_2SO_4. d) Time-dependence of the cathodic current density of nano-FeS_2-RGO during electrolysis under a constant overpotential of 170 mV in 0.5 M H_2SO_4. e) The configurations of hydrogen adsorption on the different FeS_2 surfaces (left (100), middle (111), and right (211)) and the corresponding free energy. In the case of (100), there are two equal S-sites for the HER process and the free energies are 0.15 and –0.15 eV for the first and second hydrogen. The black boxes denote the used supercells.

dichalcogenides as highly efficient and stable earth-abundant catalysts for HER. Starting from raw graphite and iron pyrite minerals, high-density FeS_2 nanoparticles are in situ formed and uniformly distributed within the RGO in a short time (≈12 ms) through current-induced high temperatures up to ≈2470 K. The as-synthesized ultrafine FeS_2 nanoparticles embedded in between RGO exhibit excellent HER electrocatalytic activity achieving 10 mA cm^{-2} current at overpotentials as low as 139 mV versus a reversible hydrogen electrode with superior durability. These results are among the most active earth-abundant HER electrocatalysts reported in the literature. The exceptional electrocatalytic activity can be attributed to the chemical composition and structure of the ultrafine nanoparticles, as well as their robust interaction with RGO. We envision that the facile synthesis strategy can be applied to other transition metal binary, ternary, or multicomponent compounds and alloys, thus inspiring new avenues to develop highly active earth-abundant catalysts for a variety of scalable energy conversion applications.

3. Experimental Section

Materials Synthesis: In a typical synthesis, 10 mg of iron pyrite powders were obtained either from bulk pyrite minerals after being broken by a hammer or from commercial micro-sized FeS_2 powders (99.8%, ≈325 mesh). The iron pyrite powder was added to deionized water and sonicated at room temperature for 1 min. After that, 10 mg of graphene oxide ink (3 mg mL^{-1}) synthesized by a modified Hummer's method was mixed with the above solution. The obtained mixed solution was sealed and sonicated for 10 min followed by vacuum filtration. The FeS_2-GO film then could be detached from the 0.65 µm pore-sized membrane (Millipore, U.S.A) as a freestanding film after drying overnight in air. The freestanding FeS_2-GO film was then preannealed in a tube furnace at 573 K for 1 h under Argon atmosphere, reducing the FeS_2-GO to FeS_2-RGO, to trigger the current induced thermal shock. After high-temperature thermal shock treatment at ≈2470 K, the as-synthesized FeS_2-RGO film was cut into small pieces (6 × 6 mm^2 in size) for further electrochemical measurements. All chemicals were purchased from Sigma-Aldrich and used as received.

Thermal Shock Treatment: The freestanding FeS_2-RGO film was mounted on a substrate of glass slides with a gap. Copper ribbons were employed as the connecting wires to the external circuit and silver paste (SPI supplies) was applied to both ends of the FeS_2-RGO film as electrodes to ensure contact between the film and copper ribbons. The thermal shock treatment was achieved by applying an ultrafast current or voltage pulse within a short timespan to the premounted FeS_2-RGO film in a vacuum chamber. A specially designed sub-millisecond diagnostic system monitored the real-time temperature during the process. A 0.5 m spectroscope (Acton SP 500i), which had a 150 l mm^{-1} grating to disperse the light, was used to collect the light emission from the film during the thermal shock. The obtained spectrum was generated by a 32 channel PMT array interfaced with a high-speed data acquisition system (Vertilon IQSP 580). The data acquisition was carried over the wavelength range of 505–811 nm. In order to sufficiently resolve the sub-millisecond thermal shock, the sample rate on the acquisition system is set to 10 000 Hz, i.e., producing a sample every 100 µs. With temperature as a free parameter, the spectrum was subsequently fit to the blackbody radiation equation using Planck's law to obtain the monitored temperature profile.

Materials Characterizations: The morphology of as-prepared FeS_2-RGO electrocatalyst was characterized by a Hitachi SU-70 field emission scanning electron microscope (SEM) with EDX under an accelerating voltage of 15 kV. TEM images were taken by a JEOL JEM 2100F operated at an accelerating voltage of 200 kV and equipped with a high angle annular dark field detector in scanning TEM mode and an Oxford Inca EDX detector. XPS measurements were taken using a Kratos Axis 165 X-ray photoelectron spectrometer. XRD measurement was taken using the D8 Advanced (Bruker AXS, WI, USA).

Electrochemical Measurements: All electrochemical measurements were conducted at room temperature, 298 K, in air. The electrochemical

© 2017 WILEY-VCH Verlag GmbH & Co. KGaA, Weinheim

tests for HER were performed in a standard three-electrode setup and recorded using a Bio-Logic EC-Lab electrochemistry tester. The nano-FeS_2-RGO sample was directly employed as a working electrode, meanwhile platinum foil and commercial Ag/AgCl electrode were selected as the counter and reference electrode, respectively. A linear sweep voltammetry was measured in the 0.5 M H_2SO_4 electrolyte at a scan rate of 2 mV s^{-1} to obtain the polarization curves and further evaluate the activity of the material. Cycle stability of nano-FeS_2-RGO electrocatalyst was performed by continuous potential sweeps at a scan rate of 50 mV s^{-1} in 0.5 M H_2SO_4. The long-term durability was also characterized by monitoring the current density during continuous hydrogen production under a constant overpotential of 170 mV.

Modeling: The Vienna ab initio simulation package (VASP)[57] was used to carry out first-principle calculations with the Perdew–Burke–Ernzerhof exchange correlation.[58] The electron–ion interaction was described by the projector augmented wave pseudopotentials[59] with the kinetic energy cutoff of 370 eV. The binding energy is defined as $E_b = E\,[FeS_2 + nH] - E[FeS_2 + (n-1)H] - ½\,E[H_2]$, where $E\,[FeS_2 + nH]$ is the total energy of n hydrogen atoms adsorbed by the FeS_2 system and $E[H_2]$ is the energy of a hydrogen molecule. Then the Gibbs free energy, ΔG, for hydrogen adsorption can be calculated.[60] Here it is simplified as $\Delta G = E_b + 0.25$ eV owing to the rather weak dependence of the hydrogen zero point energy in different adsorbed states.

Supporting Information

Supporting Information is available from the Wiley Online Library or from the author.

Acknowledgements

Y.C. and S.X. contributed equally to this work. This project was supported by the NSF Scalable Nanomanufacturing Project #1635221 (entitled "SNM: Continuous Synthesis and Stabilization of Nanoparticles in a Carbon Matrix Using Rapid Thermal Shock"). The authors acknowledge the support of the Maryland NanoCenter and its AIMLab. Y.C. would like to acknowledge the China Scholarship Council (CSC) for financial support. The work at NCNST of Y.L. was supported by the National Natural Science Foundation of China (Grant No. 11674071). Partial support for M.R.Z. and R.J.J. came from an ONR-MURI grant.

Conflict of Interest

The authors declare no conflict of interest.

Keywords

2D materials, catalysis, FeS_2 nanoparticles, ultrafast, water splitting

Received: February 22, 2017
Revised: April 12, 2017
Published online: July 10, 2017

[1] C. Liu, J. Tang, H. M. Chen, B. Liu, P. Yang, *Nano Lett.* **2013**, *13*, 2989.
[2] M. S. Dresselhaus, I. L. Thomas, *Nature* **2001**, *414*, 332.
[3] Y. Lin, G. Yuan, S. Sheehan, S. Zhou, D. Wang, *Energy Environ. Sci.* **2011**, *4*, 4862.
[4] H. Zhang, Q. Ding, D. He, H. Liu, W. Liu, Z. Li, B. Yang, X. Zhang, L. Lei, S. Jin, *Energy Environ. Sci.* **2016**, *9*, 3113.
[5] S. Hu, C. Xiang, S. Haussener, A. D. Berger, N. S. Lewis, *Energy Environ. Sci.* **2013**, *6*, 2984.
[6] Y. Li, H. Zhang, M. Jiang, Y. Kuang, H. Wang, X. Sun, *J. Mater. Chem. A* **2016**, *4*, 13731.
[7] W. Liu, E. Hu, H. Jiang, Y. Xiang, Z. Weng, M. Li, Q. Fan, X. Yu, E. I. Altman, H. Wang, *Nat. Commun.* **2016**, *7*, 10771.
[8] H. B. Wu, B. Y. Xia, L. Yu, X.-Y. Yu, X. W. (David) Lou, *Nat. Commun.* **2015**, *6*, 6512.
[9] X. Zou, Y. Zhang, *Chem. Soc. Rev.* **2015**, *44*, 5148.
[10] X. Li, X. Hao, A. Abudula, G. Guan, *J. Mater. Chem. A* **2016**, *4*, 11973.
[11] Q. Lu, Y. Yu, Q. Ma, B. Chen, H. Zhang, *Adv. Mater.* **2016**, *28*, 1917.
[12] M. S. Faber, R. Dziedzic, M. A. Lukowski, N. S. Kaiser, Q. Ding, S. Jin, *J. Am. Chem. Soc.* **2014**, *136*, 10053.
[13] L. Lai, J. R. Potts, D. Zhan, L. Wang, C. K. Poh, C. Tang, H. Gong, Z. Shen, J. Lin, R. S. Ruoff, *Energy Environ. Sci.* **2012**, *5*, 7936.
[14] D. W. Boukhvalov, Y. W. Son, R. S. Ruoff, *ACS Catalysis* **2014**, *4*, 2016.
[15] X. Cui, P. Ren, D. Deng, J. Deng, X. Bao, *Energy Environ. Sci.* **2016**, *9*, 123.
[16] J. Deng, P. Ren, D. Deng, L. Yu, F. Yang, X. Bao, *Energy Environ. Sci.* **2014**, *7*, 1919.
[17] J. Zhang, L. Qu, G. Shi, J. Liu, J. Chen, L. Dai, *Angew. Chem., Int. Ed Engl.* **2016**, *55*, 2230.
[18] C. Hu, L. Dai, *Adv. Mater.* **2016**, *29*, 1604942.
[19] H. Wang, C. Tsai, D. Kong, K. Chan, F. Abild-Pedersen, J. K. Nørskov, Y. Cui, *Nano Res.* **2015**, *8*, 566.
[20] J. Xie, H. Zhang, S. Li, R. Wang, X. Sun, M. Zhou, J. Zhou, X. W. (David) Lou, Y. Xie, *Adv. Mater.* **2013**, *25*, 5807.
[21] J.-S. Li, Y. Wang, C.-H. Liu, S.-L. Li, Y.-G. Wang, L.-Z. Dong, Z.-H. Dai, Y.-F. Li, Y.-Q. Lan, *Nat. Commun.* **2016**, *7*, 11204.
[22] Y. Li, H. Wang, L. Xie, Y. Liang, G. Hong, H. Dai, *J. Am. Chem. Soc.* **2011**, *133*, 7296.
[23] J. Deng, H. Li, J. Xiao, Y. Tu, D. Deng, H. Yang, H. Tian, J. Li, P. Ren, X. Bao, *Energy Environ. Sci.* **2015**, *8*, 1594.
[24] D. Merki, H. Vrubel, L. Rovelli, S. Fierro, X. Hu, *Chem. Sci.* **2012**, *3*, 2515.
[25] D. Merki, S. Fierro, H. Vrubel, X. Hu, *Chem. Sci.* **2011**, *2*, 1262.
[26] D. Kong, H. Wang, J. J. Cha, M. Pasta, K. J. Koski, J. Yao, Y. Cui, *Nano Lett.* **2013**, *13*, 1341.
[27] M. A. Lukowski, A. S. Daniel, C. R. English, F. Meng, A. Forticaux, R. J. Hamers, S. Jin, *Energy Environ. Sci.* **2014**, *7*, 2608.
[28] D. Voiry, H. Yamaguchi, J. Li, R. Silva, D. C. B. Alves, T. Fujita, M. Chen, T. Asefa, V. B. Shenoy, G. Eda, M. Chhowalla, *Nat. Mater.* **2013**, *12*, 850.
[29] A. T. Garcia-Esparza, D. Cha, Y. Ou, J. Kubota, K. Domen, K. Takanabe, *ChemSusChem* **2013**, *6*, 168.
[30] H. Wang, D. Kong, P. Johanes, J. J. Cha, G. Zheng, K. Yan, N. Liu, Y. Cui, *Nano Lett.* **2013**, *13*, 3426.
[31] M. Cabán-Acevedo, M. L. Stone, J. R. Schmidt, J. G. Thomas, Q. Ding, H.-C. Chang, M.-L. Tsai, J.-H. He, S. Jin, *Nat. Mater.* **2015**, *14*, 1245.
[32] W. Liu, E. Hu, H. Jiang, Y. Xiang, Z. Weng, M. Li, Q. Fan, X. Yu, E. I. Altman, H. Wang, *Nat. Commun.* **2016**, *7*, 10771.
[33] H. Wang, H.-W. Lee, Y. Deng, Z. Lu, P.-C. Hsu, Y. Liu, D. Lin, Y. Cui, *Nat. Commun.* **2015**, *6*, 7261.
[34] L.-L. Feng, G. Yu, Y. Wu, G.-D. Li, H. Li, Y. Sun, T. Asefa, W. Chen, X. Zou, *J. Am. Chem. Soc.* **2015**, *137*, 14023.
[35] Z. Pu, Q. Liu, C. Tang, A. M. Asiri, X. Sun, *Nanoscale* **2014**, *6*, 11031.
[36] W.-F. Chen, K. Sasaki, C. Ma, A. I. Frenkel, N. Marinkovic, J. T. Muckerman, Y. Zhu, R. R. Adzic, *Angew. Chem., Int. Ed.* **2012**, *51*, 6131.
[37] J. R. McKone, B. F. Sadtler, C. A. Werlang, N. S. Lewis, H. B. Gray, *ACS Catal.* **2013**, *3*, 166.

 © 2017 WILEY-VCH Verlag GmbH & Co. KGaA, Weinheim

[38] H. Wang, Z. Lu, D. Kong, J. Sun, T. M. Hymel, Y. Cui, *ACS Nano* **2014**, *8*, 4940.
[39] M. Cabán-Acevedo, N. S. Kaiser, C. R. English, D. Liang, B. J. Thompson, H.-E. Chen, K. J. Czech, J. C. Wright, R. J. Hamers, S. Jin, *J. Am. Chem. Soc.* **2014**, *136*, 17163.
[40] M. S. Faber, M. A. Lukowski, Q. Ding, N. S. Kaiser, S. Jin, *J. Phys. Chem. C* **2014**, *118*, 21347.
[41] M. Cabán-Acevedo, M. S. Faber, Y. Tan, R. J. Hamers, S. Jin, *Nano Lett.* **2012**, *12*, 1977.
[42] D. Susac, L. Zhu, M. Teo, A. Sode, K. C. Wong, P. C. Wong, R. R. Parsons, D. Bizzotto, K. A. R. Mitchell, S. A. Campbell, *J. Phys. Chem. C* **2007**, *111*, 18715.
[43] A. Douglas, R. Carter, L. Oakes, K. Share, A. P. Cohn, C. L. Pint, *ACS Nano* **2015**, *9*, 11156.
[44] D. Kong, J. J. Cha, H. Wang, H. R. Lee, Y. Cui, *Energy Environ. Sci.* **2013**, *6*, 3553.
[45] Y. Zhu, S. Murali, W. Cai, X. Li, J. W. Suk, J. R. Potts, R. S. Ruoff, *Adv. Mater.* **2010**, *22*, 3906.
[46] D. C. Marcano, D. V. Kosynkin, J. M. Berlin, A. Sinitskii, Z. Sun, A. Slesarev, L. B. Alemany, W. Lu, J. M. Tour, *ACS Nano* **2010**, *4*, 4806.
[47] T. Rosenqvist, *Principles of Extractive Metallurgy*, Tapir Academic Press, New York. **2004**.
[48] Y. Su, V. G. Kravets, S. L. Wong, J. Waters, A. K. Geim, R. R. Nair, *Nat. Commun.* **2014**, *5*, 4843.
[49] J. Xie, W. Song, G. Cao, T. Zhu, X. Zhao, S. Zhang, *RSC Adv.* **2014**, *4*, 7703.
[50] C. Chen, M. Long, M. Xia, C. Zhang, W. Cai, *Nanoscale Res. Lett.* **2012**, *7*, 101.
[51] M. Wang, C. Xing, K. Cao, L. Zhang, J. Liu, L. Meng, *J. Mater. Chem. A* **2014**, *2*, 9496.
[52] B. Li, L. Huang, M. Zhong, Z. Wei, J. Li, *RSC Adv.* **2015**, *5*, 91103.
[53] Y. Wang, B. Chen, D. H. Seo, Z. J. Han, J. I. Wong, K. (Ken) Ostrikov, H. Zhang, H. Y. Yang, *NPG Asia Mater.* **2016**, *8*, e268.
[54] B. Konkena, K. junge Puring, I. Sinev, S. Piontek, O. Khavryuchenko, J. P. Dürholt, R. Schmid, H. Tüysüz, M. Muhler, W. Schuhmann, U.-P. Apfel, *Nat. Commun.* **2016**, *7*, 12269.
[55] J. Miao, F.-X. Xiao, H. B. Yang, S. Y. Khoo, J. Chen, Z. Fan, Y.-Y. Hsu, H. M. Chen, H. Zhang, B. Liu, *Sci. Adv.* **2015**, *1*, e1500259.
[56] C.-B. Ma, X. Qi, B. Chen, S. Bao, Z. Yin, X.-J. Wu, Z. Luo, J. Wei, H.-L. Zhang, H. Zhang, *Nanoscale* **2014**, *6*, 5624.
[57] G. Kresse, J. Furthmüller, *Phys. Rev. B: Condens. Matter Mater. Phys.* **1996**, *54*, 11169.
[58] J. P. Perdew, K. Burke, M. Ernzerhof, *Phys. Rev. Lett.* **1996**, *77*, 3865.
[59] P. E. Blöchl, *Phys. Rev. B* **1994**, *50*, 17953.
[60] B. Hinnemann, P. G. Moses, J. Bonde, K. P. Jørgensen, J. H. Nielsen, S. Horch, I. Chorkendorff, J. K. Nørskov, *J. Am. Chem. Soc.* **2005**, *127*, 5308.

© 2017 WILEY-VCH Verlag GmbH & Co. KGaA, Weinheim